

9-1-2003

Simulating quantum transport in nanoscale MOSFETs: Ballistic hole transport, subband engineering and boundary conditions

Ramesh Venugopal
Purdue University

Zhibin Ren
IBM SRDC, Microelectronics Division

Mark S. Lundstrom
School of Electrical and Computer Engineering, Birck Nanotechnology Center, Purdue University, lundstro@purdue.edu

Follow this and additional works at: <http://docs.lib.purdue.edu/nanodocs>

Venugopal, Ramesh; Ren, Zhibin; and Lundstrom, Mark S., "Simulating quantum transport in nanoscale MOSFETs: Ballistic hole transport, subband engineering and boundary conditions" (2003). *Other Nanotechnology Publications*. Paper 40.
<http://docs.lib.purdue.edu/nanodocs/40>

This document has been made available through Purdue e-Pubs, a service of the Purdue University Libraries. Please contact epubs@purdue.edu for additional information.

Simulating Quantum Transport in Nanoscale MOSFETs: Ballistic Hole Transport, Subband Engineering and Boundary Conditions

Ramesh Venugopal, Zhibin Ren, and Mark S. Lundstrom, *Fellow, IEEE*

Abstract—We present a modeling scheme for simulating ballistic hole transport in thin-body fully depleted silicon-on-insulator pMOSFETs. The scheme includes all of the quantum effects associated with hole confinement and also accounts for valence band nonparabolicity approximately. This simulator is used to examine the effects of hole quantization on device performance by simulating a thin (1.5-nm) and thick (5-nm) body double-gated pMOSFET in the ballistic limit. Two-dimensional electrostatic effects such as drain-induced barrier lowering (DIBL) and off-equilibrium transport are emphasized as part of this study. The effect of channel orientation on the device performance is examined by simulating pMOSFETs with channels directed along $\langle 100 \rangle$ and $\langle 110 \rangle$. Simulated device characteristics for identical nMOSFETs and pMOSFETs are compared in order to explore the effects of subband engineering on CMOS technology. Novel floating boundary conditions used in simulating ballistic transport are highlighted and discussed.

Index Terms—Ballistic transport, boundary conditions, subband engineering.

I. INTRODUCTION

RECENT industrial trends indicate that the silicon-on-insulator (SOI) geometry, with its inherently improved short-channel immunity, could be the device structure that drives CMOS technology in the future [1], [2]. Also, CMOS scaling trends have progressed to a point where it is of interest to assess the ultimate performance limits of nanoscale transistors [3]. In this regard, several papers examining the ballistic limits of n-channel SOI transistors have been published recently [4]–[6]. A comprehensive analysis of p-channel transistors has yet to be reported because of the complicated band structure for holes. Therefore, our objectives are to describe a two-dimensional (2-D) simulator which is capable of modeling ballistic hole transport in thin-body SOI pMOSFETs including the effect of hole band nonparabolicity and to use this simulator to explore subband engineering for pMOSFETs. Since boundary conditions require special care for ballistic simulations, we also

discuss the boundary conditions used in this paper and in our previous work [4].

As the channel length is reduced from one transistor generation to the next, it becomes necessary to reduce the SOI film thickness in order to maintain a tolerable degree of short-channel effect, i.e., threshold voltage rolloff and drain-induced barrier lowering (DIBL) [7]. Reducing the SOI film thickness causes the carriers in the inversion layer to be distributed over fewer subbands. This, in turn, substantially affects the electrical characteristics of short-channel SOI MOSFETs. Recent studies have presented strategies to enhance the performance of n-channel SOI MOSFETs by utilizing this subband structure [8]. However, such subband engineering cannot be performed for n-channel devices in isolation, and it is of interest to see how carrier quantization affects the performance of pMOSFETs. Therefore, we use our 2-D simulator for holes to examine the effects of subband engineering in ultra-thin-body pMOSFETs. The importance of 2-D electrostatic effects such as DIBL and off-equilibrium transport are emphasized as part of this study. Simulated device performance for pMOSFETs is compared against the performance of identical nMOSFETs in order to provide a clear perspective of subband engineering in thin-body SOI transistors at the ballistic limit.

This paper is organized as follows. Section II outlines the modeling scheme. Section III presents simulation results for n and p channel MOSFETs with identical device geometries. Section IV discusses the special boundary conditions that have been used to model ballistic transport and Section V summarizes key findings.

II. THEORY

In this section, we present the self-consistent 2-D solution scheme that has been used to evaluate the hole distribution and source-to-drain current in thin-body fully depleted ballistic (no scattering) pMOSFETs. Quantum confinement and band nonparabolicity effects are included in the solution scheme. The simulated device structure is an idealized drain-gate (DG) MOSFET with the Si/SiO₂ interface perpendicular to the $\langle 100 \rangle$ direction (Fig. 1). The y dimension is treated as infinite and the potential is assumed to be translationally invariant in the y direction. A grid spacing of a (0.4 nm) along the x direction and b (0.15 nm) along the z direction has been used in this simulation study.

Manuscript received February 25, 2003; revised April 25, 2003. This work was supported by the Semiconductor Research Corporation. This manuscript is based on a presentation at the IEEE Silicon Nanoelectronics Workshop 2002.

R. Venugopal was with the School of Electrical and Computer Engineering, Purdue University, West Lafayette, IN 47907-1285 USA. He is now with Texas Instruments, Dallas, TX 75265 USA (e-mail: ramesh.venugopal@ti.com).

Z. Ren is with the IBM SRDC, Microelectronics Division, Hopewell Junction, NY 12533 USA.

M. S. Lundstrom is with the School of Electrical and Computer Engineering, Purdue University, West Lafayette, IN 47907-1285 USA.

Digital Object Identifier 10.1109/TNANO.2003.817229

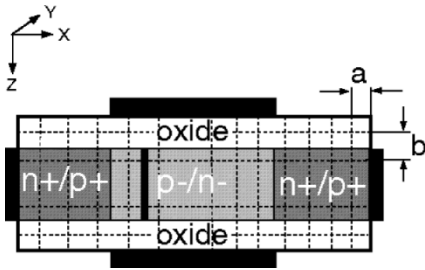


Fig. 1. Ultrathin-body DG MOSFET structure with source/drain doping of 10^{20} cm^{-3} and an intrinsic channel.

Hole transport through this idealized structure is modeled by including the effect of the warped heavy and light hole bands through the following $E-\vec{k}$ relationship

$$E(k) = \frac{-\hbar^2 k^2}{2m_0} \left[A \mp \sqrt{\left(\frac{B^2 + C^2 k_x^2 k_y^2 + k_y^2 k_z^2 + k_x^2 k_z^2}{k^4} \right)} \right] \quad (1)$$

where the negative sign represents the heavy hole and the positive sign the light hole bandstructure. A , B , and C are constants with an associated uncertainty and determined from cyclotron resonance experiments. In our analysis the A , B , and C coefficients are 4.22, 0.78, and 4.8, respectively [9]. It should be noted that in a bulk semiconductor, the light and heavy hole bands are degenerate around the $\vec{k} = 0$ point as indicated in (1). Also, in general, a nonlinear $E-\vec{k}$ relationship for holes implies a nonzero, \vec{k} dependent coupling between the light and heavy hole bands. To include these coupling effects accurately, a 6×6 Hamiltonian operator that is \vec{k} dependent needs to be discretized in two dimensions [10]. Such a solution is computationally expensive because of the size of the Hamiltonian and the associated \vec{k} -space grid. Therefore, to reduce the computational cost and at the same time capture the essential physics of ballistic hole transport including the effect of nonparabolicity, we use simplifying but physical approximations.

To explain the solution scheme we focus our attention on a thin z directed vertical slice at a fixed x location within the device, as shown in Fig. 1. Carriers within this slice are strongly quantum confined along z and reside in a discrete set of subbands. The effect of strong quantum confinement is the removal of the degeneracy between the light and heavy hole bands around the $\vec{k} = 0$ point (k_z discrete) and an increased separation between adjacent subbands away from the $\vec{k} = 0$ point. Therefore, in modeling hole transport in ultra-thin-body transistors, we assume that the separation between adjacent subbands is large enough (strong confinement) to ignore band-to-band coupling. Also, by focusing on the valence band maximum ($k_x = k_y = 0$), individual subband energies and their corresponding wave functions (envelope) can be obtained by solving a one-dimensional (1D), z directed, single band effective mass equation of the form,

$$\frac{\hbar^2}{2m_z^*} \frac{\partial^2 \Psi_i(x, z)}{\partial z^2} - qV(x, z)\Psi_i(x, z) = E_i(x)\Psi_i(x, z). \quad (2)$$

In (2), m_z^* is the effective mass along the confinement direction, $E_i(x)$ and $\Psi_i(x, z)$ are the the eigen energies and wavefunctions

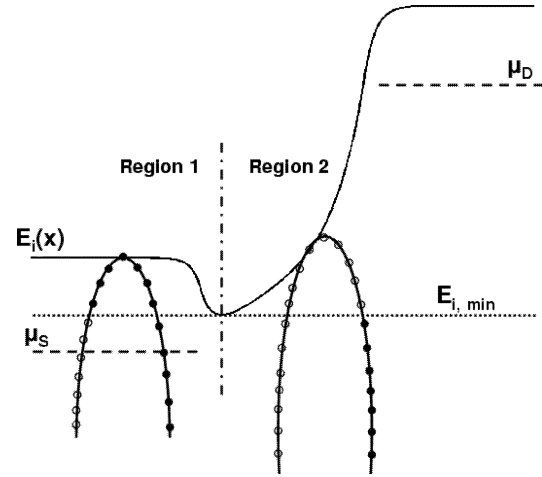


Fig. 2. Pictorial representation of the Boltzmann solution for a generic hole subband. Filled circles represent states that are filled by the source Fermi level (μ_S) and empty circles represent states filled by the drain Fermi level (μ_D).

for subband i , at slice x and $V(x, z)$ is the 2-D potential profile. The effective mass used in (2) is,

$$m_z^* = \frac{m_0}{A \mp B} \quad (3)$$

where the negative sign represents the heavy hole and the positive sign the light hole band respectively. Note that Ψ_i in (2) is indeed the envelope function for holes along the gate confinement direction. In deriving (2), we restricted our focus to the valence band maximum ($k_x = k_y = 0$), thereby eliminating the complex band warping and coupling present in the valence band. Therefore, the reciprocal effective mass tensor becomes a diagonal matrix for the heavy and light hole bands. This approximation of a parabolic band structure for holes in the confinement direction, enables us decouple the channel and confinement directions thus greatly reducing the associated computational burden [11]. It has been shown to work well for double-gate MOSFETs [12]. Note that the warped $E(k_x, k_y)$ surface ($k_z = 0$ in (1)) associated with each hole subband includes the essential characteristics of the corresponding $E(k_x, k_y)$ relationship obtained from a more general calculation based on the Luttinger Hamiltonian within the energy range of interest [10]. These approximations and the band structure used in this analysis have also been shown to reproduce measured $C-V$ characteristics of pMOS capacitors accurately in the literature [13].

A solution to (2) at every x location within the device yields a set of subband profiles. Since coupling between different subbands is ignored and the transport is ballistic, a 1D Boltzmann solution can be directly solved to obtain the charge density and current contribution from each subband. The Boltzmann solution technique for a generic subband profile is illustrated in Fig. 2. The subband is coupled to the source and drain reservoirs which are characterized by their Fermi levels μ_S and μ_D respectively. It should be noted that the subband energy is the effective potential energy of the hole and that holes flow up the potential hill unlike electrons. The subband profile shown in Fig. 2 can be spatially resolved into two regions: 1) points to the left of the subband minimum ($E_{i,\min}$) and 2) points to the right of the subband minimum. In region 1, holes injected from the source reservoir with x directed energies greater than $E_{i,\min}$ are

reflected off the source-to-channel barrier. Therefore, both the $+k_x$ and the $-k_x$ states representing x directed energies greater than $E_{i,\min}$ are in equilibrium with the source (filled circles in Fig. 2). Holes with x directed energies less than $E_{i,\min}$ are not reflected by the source-to-channel barrier in the Boltzmann picture. Since there is no barrier reflection and the transport is ballistic, the $+k_x$ states are in equilibrium with the source (filled circles in Fig. 2) and the $-k_x$ states are in equilibrium with the drain (empty circles in Fig. 2) for x directed energies less than $E_{i,\min}$. A similar analysis applies for holes in region 2.

The charge density within a device is primarily determined by electrostatics. Therefore, when evaluating the 2-D hole density (given a subband profile), we assume that the $E(k_x, k_y)$ relationship for the heavy and the light hole subbands is parabolic and is characterized by a mass that yields the same 2-D density of states (DOS) as the corresponding nonparabolic $E(k_x, k_y)$ relation [$k_z = 0$ in (1)]. This approximation, is necessary to obtain analytical expressions for the charge density as outlined in the subsequent paragraph. The 2-D DOS effective mass can be expressed as [14]

$$m_d^* = \frac{m_0}{2\pi} \int_0^{2\pi} \frac{d\theta}{\left[A \mp \sqrt{(B^2 + C^2 \cos^2 \theta \sin^2 \theta)} \right]} \quad (4)$$

where, θ is the polar angle in the $k_x - k_y$ plane. Using this mass and the incidence and reflection arguments illustrated in Fig. 2, the 2-D hole density in region 1 can be expressed as,

$$p_1(x) = p_{2-D,i} \left[\begin{aligned} & \ln(1 + e^{-\tilde{\mu}_S}) \\ & + \frac{1}{\sqrt{\pi}} \int_0^{\tilde{E}_{i,\min}} \frac{-d\tilde{E}_x}{\sqrt{-\tilde{E}_x}} \mathfrak{F}_{-1/2}(\tilde{E}_x - \tilde{\mu}_S) \\ & + \ln(1 + e^{-\tilde{\mu}_D}) \\ & - \frac{1}{\sqrt{\pi}} \int_0^{\tilde{E}_{i,\min}} \frac{-d\tilde{E}_x}{\sqrt{-\tilde{E}_x}} \mathfrak{F}_{-1/2}(\tilde{E}_x - \tilde{\mu}_D) \end{aligned} \right] \quad (5)$$

Both Fermi-Dirac statistics and spin degeneracy have been included in (5). Note that all energies in (5) have been normalized by $k_B T$ and that the tilde implies that the energies are specified relative to the local subband energy $E_i(x)$. The 2-D density factor for subband i ($p_{2-D,i}$) is $m_{d,i}^* k_B T / 2\pi \hbar^2$. A similar expression for the 2-D hole density in region 2 can be obtained.

$$p_2(x) = p_{2-D,i} \left[\begin{aligned} & \ln(1 + e^{-\tilde{\mu}_S}) \\ & - \frac{1}{\sqrt{\pi}} \int_0^{\tilde{E}_{i,\min}} \frac{-d\tilde{E}_x}{\sqrt{-\tilde{E}_x}} \mathfrak{F}_{-1/2}(\tilde{E}_x - \tilde{\mu}_S) \\ & + \ln(1 + e^{-\tilde{\mu}_D}) \\ & + \frac{1}{\sqrt{\pi}} \times \int_0^{\tilde{E}_{i,\min}} \frac{-d\tilde{E}_x}{\sqrt{-\tilde{E}_x}} \mathfrak{F}_{-1/2}(\tilde{E}_x - \tilde{\mu}_D) \end{aligned} \right] \quad (6)$$

This 2-D charge density is distributed along the confinement direction at each x location using the corresponding wave function $|\Psi_i(z)|^2/b$ in order to obtain the 3D density profile. A summation over all the subbands yields the final charge density that is input to the Poisson solver for self-consistent solutions. Note that this treatment captures all of the quantum effects associated with hole confinement and can also treat the effect of hole wavefunction penetration into the insulator regions.

A nonlinear version of the Poisson equation which uses floating boundaries (Section IV) is solved in order to expedite convergence between the Poisson and transport iterations. Nonlinearity is forced into the Poisson equation by expressing the three-dimensional (3-D) hole density in terms of a corresponding quasi-Fermi level at each node of the 2-D grid using

$$p(x, z) = N_V \mathfrak{F}_{1/2} \left[\frac{-qV_{\text{old}} - F_p}{k_B T} \right]$$

and

$$F_p = -qV_{\text{old}} - k_B T \mathfrak{F}_{1/2}^{-1} \left[\frac{p}{N_V} \right] \quad (7)$$

where N_V is the effective DOS in the valence band, V_{old} is the potential from the previous iteration, and $\mathfrak{F}_{-1/2}^{-1}$ is the inverse Fermi integral of order $-1/2$ [15]. Details of the nonlinear technique to solve Poisson's equation can be found in [16]–[18]. The maximum difference in potential between successive iterations is used as a measure of convergence.

Once convergence is achieved, the terminal current can be evaluated at any point within the device, because it is a conserved quantity. We evaluate the current at the bottom of the source-to-channel barrier ($E_{i,\min}$ point in Fig. 2) because this is a point where there is no reflection. Since this is a one-time calculation, the terminal current, including the effect of band nonparabolicity, is obtained by explicitly summing fluxes in \vec{k} -space. It should be noted that although the confinement direction is $\langle 100 \rangle$, the channel could be oriented along either the $\langle 100 \rangle$ or the $\langle 110 \rangle$ direction. Therefore, the occupancy factor (Fermi function) associated with a specific \vec{k} -state needs to be correctly defined. If the channel is oriented along $\langle 100 \rangle$, all $+k_x$ states are filled using μ_S and the $-k_x$ states are filled using μ_D . However, if the channel orientation is changed to $\langle 110 \rangle$, we perform a 45° rotation of the (k_x, k_y) axis to obtain a modified 2-D $E(k'_x, k'_y)$ relation. In this new orientation, all of the $+k'_x$ states are filled using μ_S and the $-k'_x$ states are filled using μ_D given the subband minimum. The expression for the current density from subband i including spin degeneracy is

$$I_i = \frac{q}{2\pi^2} \left[\int_{-\infty}^{\infty} \int_0^{\infty} \frac{\vec{v}(k_x, k_y) dk_x dk_y}{1 + \exp\left(\frac{\mu_S - (E(k_x, k_y) + E_{i,\min})}{k_B T}\right)} - \int_{-\infty}^{\infty} \int_0^{\infty} \frac{\vec{v}(k_x, k_y) dk_x dk_y}{1 + \exp\left(\frac{\mu_D - (E(k_x, k_y) + E_{i,\min})}{k_B T}\right)} \right] \quad (8)$$

Note that the velocity in (8) includes the direction dependence associated with a specific channel orientation. Summing each subband contribution yields the total terminal current for a

particular channel orientation. Analogous expressions for the charge density and current in ultra-thin-body fully depleted nMOSFETs were presented in [18].

III. RESULTS

In this section, we compare the ballistic performance of two ultra-thin-body n- and pMOSFETs. The first device has a silicon body thickness of 1.5 nm and the second device has a body thickness of 5 nm. Both devices have the geometry shown in Fig. 1 with a source/drain doping of 10^{20} cm^{-3} and an intrinsic channel. The junctions are abrupt and the oxide thickness is 1.5 nm. In order to minimize short-channel effects, a channel length of 20 nm has been assumed in all of the simulations. A power supply voltage V_{DD} of 0.6 V is used, and, to facilitate performance comparison, the threshold voltage (current value = $1 \mu\text{A}/\mu\text{m}$) of each device is calibrated to $0.25 V_{DD}$ by adjusting the gate work function. Electron and hole wave function penetration into the insulator regions is not considered, and the focus is primarily on the ON state ($V_{GS} = V_{DS} = V_{DD}$).

The ballistic current is a product of the charge density and the carrier velocity. The charge density within a device is primarily prescribed by 2-D electrostatics and the velocity (for a given charge density) by the band structure. Therefore, the effects of 2-D electrostatics and band structure on device performance can be explained by examining the charge density and carrier velocity at a point within the device. We examine these quantities at the “charge control point.” To illustrate the charge control point, we plot the 2-D potential and subband profiles within the 1.5-nm body nMOSFET and pMOSFET structures in the ON state (Fig. 3). Although the potential profile is a 2-D function (x and z dimensions), the subbands are a function of x alone and represent the effective potential energy of the confined 2-D carriers. Each subband exhibits a maximum (minimum for holes) as one moves from the source to the drain. This point is referred to as the charge control point because it is a point where there is no carrier reflection due to the potential profile. Note that due to the thin nature of the body (1.5 nm), both transistors exhibit single subband occupancy. Also note that since the effective mass ($0.98 m_0$) of the electron in the confinement direction is higher than that of the corresponding heavy hole ($m_0/A - B$), the confinement energy of the hole is higher than that of the electron (distance between E_V and the subband) is higher than that of the electron (distance between E_C and the subband).

Fig. 4 presents the ballistic current versus voltage characteristics of the 1.5-nm body nMOSFETs and pMOSFETs. Both transistors exhibit a near-ideal subthreshold swing of 61 mV/dec due to the thin-body and the double-gate geometry. Despite exhibiting identical subthreshold behavior, the ON current from the ballistic pMOSFET is only 60% of that from the ballistic nMOSFET for a channel orientation of $\langle 100 \rangle$. To explain this difference, we plot the 2-D charge density and the corresponding nonequilibrium injection velocity (derived from the current) at the charge control point in Fig. 5. It is clear from Fig. 5 that although the hole density is slightly higher than the corresponding electron density as a result of 2-D electrostatics, the hole injection velocity is considerably ($\sim 50\%$) lower than the corresponding electron velocity. This indicates that the heavy hole is indeed heavy along both the confinement and channel directions,

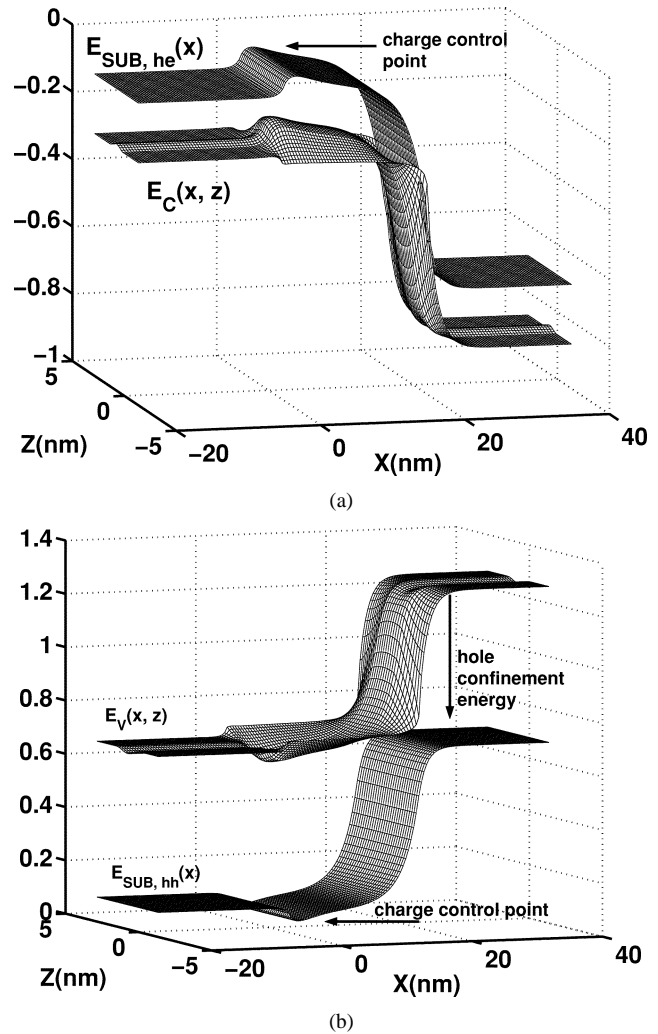


Fig. 3. (a) Conduction band and profile of the first subband in the 1.5-nm body nMOSFET (“he” represents a heavy electron in the confinement direction). (b) Valence band and profile of the first subband in the 1.5-nm body pMOSFET (“hh” represents a heavy hole in the confinement direction). All energies are referred to the source Fermi level (0). Due to the high doping in the source/drain regions, the electron subband is negative and the hole subband positive with regards to the reference. Note that the confinement energy of the hole is much higher than the electron. The bias state is $|V_{GS}| = 0.45 \text{ V}$ and $|V_{DS}| = 0.6 \text{ V}$.

unlike the heavy electron which is heavy along the confinement but light along the channel (unprimed valley, $0.19 m_0$). This analysis also indicates that in thin-body SOI devices under conditions of single subband occupancy, the ballistic pMOSFET will always largely underperform the nMOSFET irrespective of channel length scaling. Therefore, band structure engineering is essential in order to increase pMOSFET performance.

An excellent analytical analysis of ballistic device performance in thin-body DG MOSFETs assuming single subband occupancy and 1-D electrostatics has been presented in the literature [19]. We examine the validity of this 1-D treatment of the electrostatics by plotting the 2-D charge density and velocity at the charge control point as a function of $|V_{DS}|$ for the 1.5-nm body nMOSFETs and pMOSFETs (Fig. 6). In the absence of 2-D effects, the charge at the top of the barrier is determined by the gate overdrive in the ON state (evaluated at $|V_{DS}| = 0, |V_{GS}| = 0.6 \text{ V}$). On including 2-D effects, it is clear from Fig. 6 that the charge at the control point is increased as

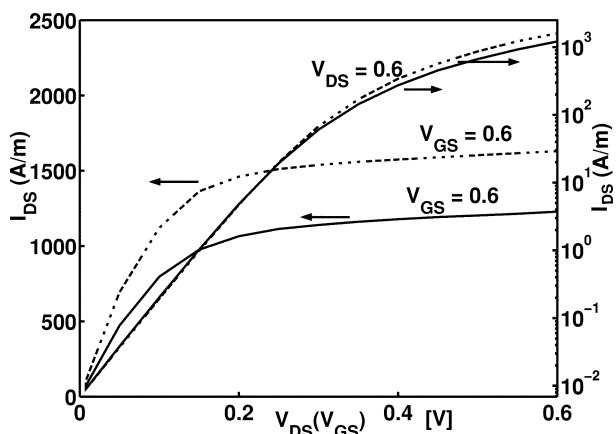


Fig. 4. I_{DS} versus V_{GS} (log scale) and I_{DS} versus V_{DS} (linear scale) characteristics of the 1.5-nm body n- (dotted line) and p- (solid line) MOSFETs for a channel orientation of $\langle 100 \rangle$. Both devices exhibit near-ideal subthreshold characteristics. The ON current of the pMOSFET is $\sim 40\%$ lower than that of the nMOSFET.

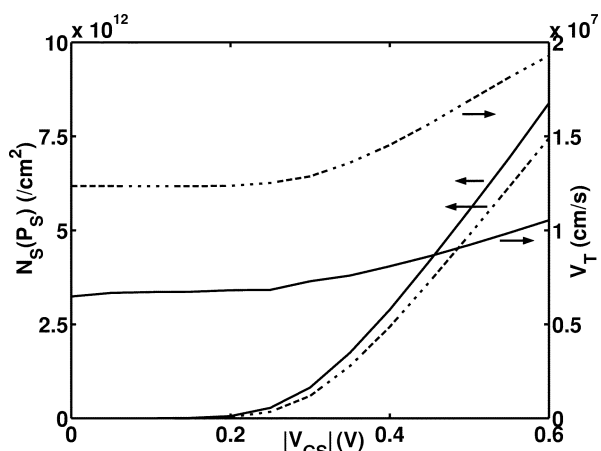


Fig. 5. 2-D charge density and injection velocity extracted at the charge control point versus V_{GS} for the 1.5-nm body n- (dotted line) and p- (solid line) MOSFETs. At the same gate voltage, the hole density is $\sim 10\%$ greater than the electron density, but the hole injection velocity along $\langle 100 \rangle$ is $\sim 50\%$ lower than the electron injection velocity due to the warped nature of the heavy hole subband.

a result of DIBL in case of both nMOSFETs and pMOSFETs. For the pMOSFET, this increase in charge density is $\sim 15\%$ despite using an ultra thin body and a relatively long channel. The charge density difference translates to an increased difference ($\sim 25\%$) in the ballistic current as a result of degeneracy (see Section IV). A similar trend is also observed in case of the nMOSFET. Note that due to degeneracy effects, the saturation nonequilibrium injection velocities for both electrons ($\sim 1.9 \times 10^7$ cm/s) and holes ($\sim 1 \times 10^7$ cm/s) are much higher than their equilibrium injection values ($\sim 1.5 \times 10^7$ cm/s for electrons and $\sim 8 \times 10^6$ cm/s for holes).

On increasing the body thickness to 5 nm, the difference between the ON currents of the nMOSFETs and pMOSFETs reduces to $\sim 25\%$ (Fig. 7). To understand this reduced difference, we focus on the 2-D charge density and injection velocity at the control point once again (Fig. 8). The injection velocity for the hole is $\sim 85\%$ of that for the electron (unlike the 1.5-nm body) and the 2-D hole density is $\sim 10\%$ less than the corresponding electron density, thus resulting in the observed difference in the

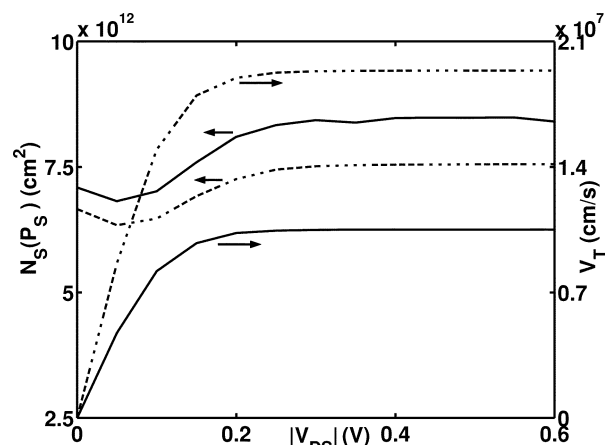


Fig. 6. 2-D charge density and injection velocity extracted at the charge control point versus V_{DS} for the 1.5-nm body n- (dotted line) and p- (solid line) MOSFETs. DIBL increases the charge density by $\sim 15\%$. Injection velocities are higher than their equilibrium values due to degeneracy (Section IV).

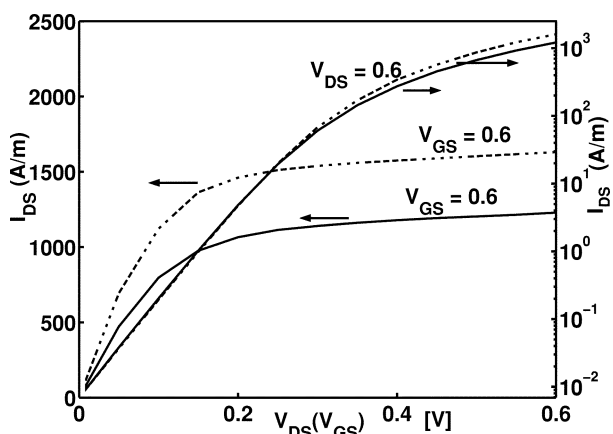


Fig. 7. I_{DS} versus V_{GS} (log scale) and I_{DS} versus V_{DS} (linear scale) characteristics of the 5-nm body n- (dotted line) and p- (solid line) MOSFETs for a channel orientation of $\langle 100 \rangle$. Both devices exhibit near-ideal subthreshold characteristics. The ON current of the pMOSFET is $\sim 25\%$ lower than that of the nMOSFET.

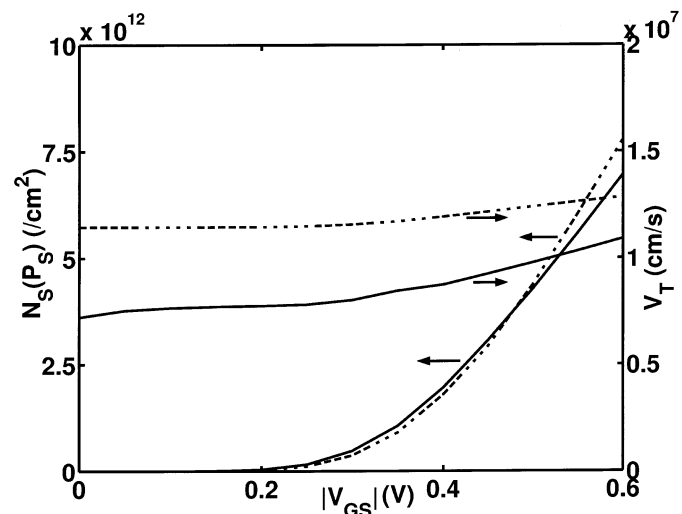


Fig. 8. 2-D charge density and injection velocity extracted at the charge control point versus V_{GS} for the 5-nm body n- (dotted line) and p- (solid line) MOSFETs. The crossover in the 2-D charge density is due to an increased inversion layer capacitance for the electrons as a result of higher subband occupancy. Note that higher subband occupancy considerably degrades the injection velocity for electrons, whereas hole velocity is relatively unaffected when compared with Fig. 5.

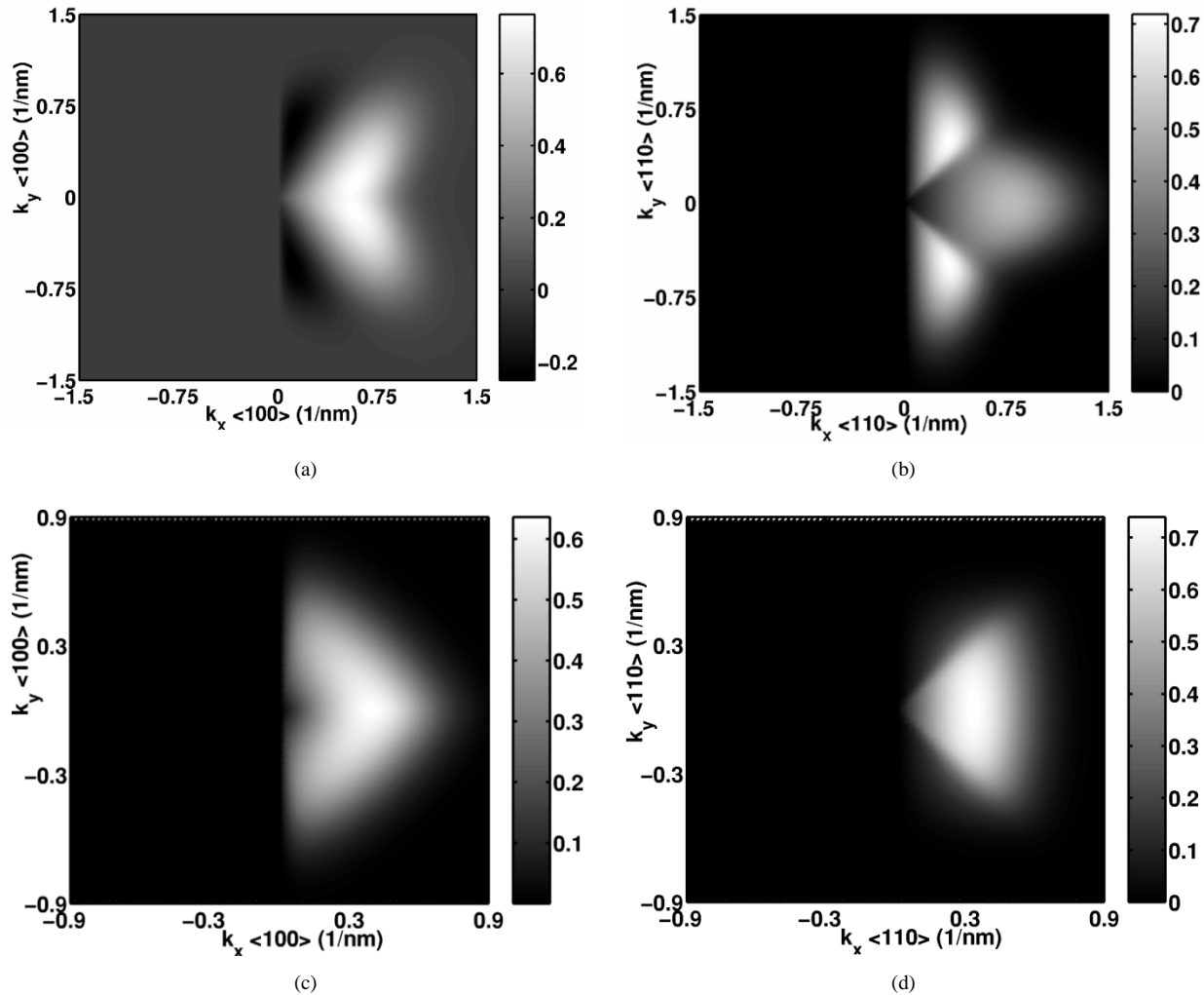


Fig. 9. (a) Flux distribution in \vec{k} -space for the heavy hole band in the 5-nm body pMOSFET along the $\langle 100 \rangle$ (left) and $\langle 110 \rangle$ (right) directions. (b) Flux distribution in \vec{k} -space for the light hole band in the 5-nm body pMOSFET along the $\langle 100 \rangle$ (left) and $\langle 110 \rangle$ (right) directions. Note that in the ON state, only one half of \vec{k} -space is occupied as drain injection is suppressed. Also, note that the k axes are rotated by 45° between the left and right pictures.

ON current. To explain this behavior of the charge density and injection velocity, we note that only $\sim 40\%$ of the inversion electron charge resides in the first unprimed subband in case of the 5-nm nMOSFET, whereas $\sim 80\%$ of the hole charge continues to occupy the first heavy hole band in the pMOSFET. Increased occupancy of the high energy subbands degrades the electron injection velocity because the average channel effective mass is increased [8]. For holes, since the light hole band is light in the confinement and channel directions, the hole injection velocity is improved slightly as the light hole population is increased, thus resulting in a reduced difference between the electron and hole injection velocities. The effective gate capacitance of the nMOSFET is greater than the pMOSFET as the effective 2-D DOS for electrons is greater than that of holes (primed bands have a higher DOS compared to the light hole band). Therefore, the inversion charge density at a high gate voltage is higher for electrons than holes (crossover point in Fig. 8 is the voltage at which high-energy subbands start contributing to the electron charge).

It should be noted that increasing the body thickness from 1.5 to 5 nm reduces the inversion layer capacitance for both the n- and pMOSFETs as the charge centroid is pushed away

from the Si/SiO₂ interface. Also, for electrons we noted that the saturation injection velocity reduced with higher subband occupancy. The net effect of the effective gate capacitance and injection velocity degradation is a $\sim 30\%$ reduction in the nMOSFET performance as we scale the body thickness from 1.5 to 5 nm. For the pMOSFET, we observed that increasing the body thickness actually increased the injection velocity slightly (for the same charge density). Therefore, the degradation in performance as we scale the body thickness from 1.5 to 5 nm is primarily due to capacitance degradation alone and is $\sim 15\%$. This indicates that pMOSFETs are less sensitive to subband engineering arising from reducing the body thickness as compared with nMOSFETs.

Finally, we examine the ON current performance of the 5-nm body pMOSFET as a function of channel orientation. Although (1) indicates that holes in the heavy hole band are heavier along $\langle 110 \rangle$ as opposed to $\langle 100 \rangle$, we find that for the same 2-D hole density, the current in the 5-nm body pMOSFET is $\sim 20\%$ higher for a $\langle 110 \rangle$ channel as compared with a $\langle 100 \rangle$ channel. To explain this behavior, we plot the net hole flux distribution in \vec{k} -space along the $\langle 100 \rangle$ (left) and $\langle 110 \rangle$ (right) directions for both the heavy and light hole bands in Fig. 9 (since the transistor

is operating in the ON state, only one half of the \vec{k} -states are occupied). Fig. 9(a) shows that most of the heavy holes are located near the $\langle 110 \rangle$ direction, and that these holes are responsible for the net flux irrespective of whether the channel is oriented along $\langle 110 \rangle$ or $\langle 100 \rangle$. Fig. 9(b) shows that the light hole flux displays the opposite trend; most of the light holes are located near the $\langle 100 \rangle$ direction. Therefore, no simple treatment of the direction dependence of the hole current is possible and one needs to explicitly sum over all the flux components in \vec{k} -space to study the effect of channel orientation.

For bulk pMOSFETs, it has been observed experimentally that the ON current for $\langle 100 \rangle$ oriented channels is $\sim 7\%$ higher than that of $\langle 110 \rangle$ oriented devices [20]. This behavior is the opposite of what we observed in our 5-nm body pMOSFET. Note that in the 5-nm body device, although $\sim 80\%$ of the hole density resides in the first heavy hole band and only $\sim 20\%$ in the first light hole band [note the maximum value on the \vec{k} axes in Fig. 9(a) and (b)], the light hole band contributes $\sim 35\%$ of the total hole current along $\langle 100 \rangle$. This clearly indicates that if the population in the light hole band is increased, the difference in the total current between the $\langle 100 \rangle$ and $\langle 110 \rangle$ directions will reduce and may even be reversed. Our simplified hole band structure ignores subband-to-subband coupling and scattering. These effects may have to be included in order to capture the physics of hole transport more accurately.

IV. DISCUSSION

In simulating ballistic transport in MOSFETs, great care must be exercised in treating the boundaries. We impose floating boundary conditions when solving Poisson's equation. This boundary condition is realized by setting

$$\hat{x} \cdot \vec{\nabla} V = 0 \quad (9)$$

at the source and drain ends of the simulation domain. Conventional transport models use fixed potential boundary conditions assuming equilibrium statistics and charge neutrality at the contacts. Under ballistic transport conditions, equilibrium statistics no longer apply [21], and our use of the floating boundary condition helps us restrict our focus to the intrinsic ballistic device without explicitly including the large scattering dominated contacts to which it is coupled. Note that the information about the drain bias (Fermi levels) is used in solving the transport equation for the hole density. Therefore, even if the potential is allowed to float, it cannot float to any arbitrary value. The potential floats relative to the source/drain Fermi levels.

To explain the floating boundary condition, we modify our idealized 1.5-nm body DG MOSFET structure by appending heavily doped ($5 \times 10^{20} \text{ cm}^{-3}$) p^{++} regions to the left and right ends of the device. The averaged valence band profile for the modified device structure under equilibrium conditions ($V_{GS} = -0.6 \text{ V}$, $V_{DS} = 0 \text{ V}$) is shown in Fig. 10(a). (This profile is obtained by weighting the valence band energy with the local charge density and integrating over the confinement direction.) The presence of the heavily doped p^{++} regions creates a large potential barrier for holes injected from the source and drain contacts. This barrier gives rise to strong reflections which maintain a near-equilibrium distribution in the p^{++} regions even when a large bias is applied to the

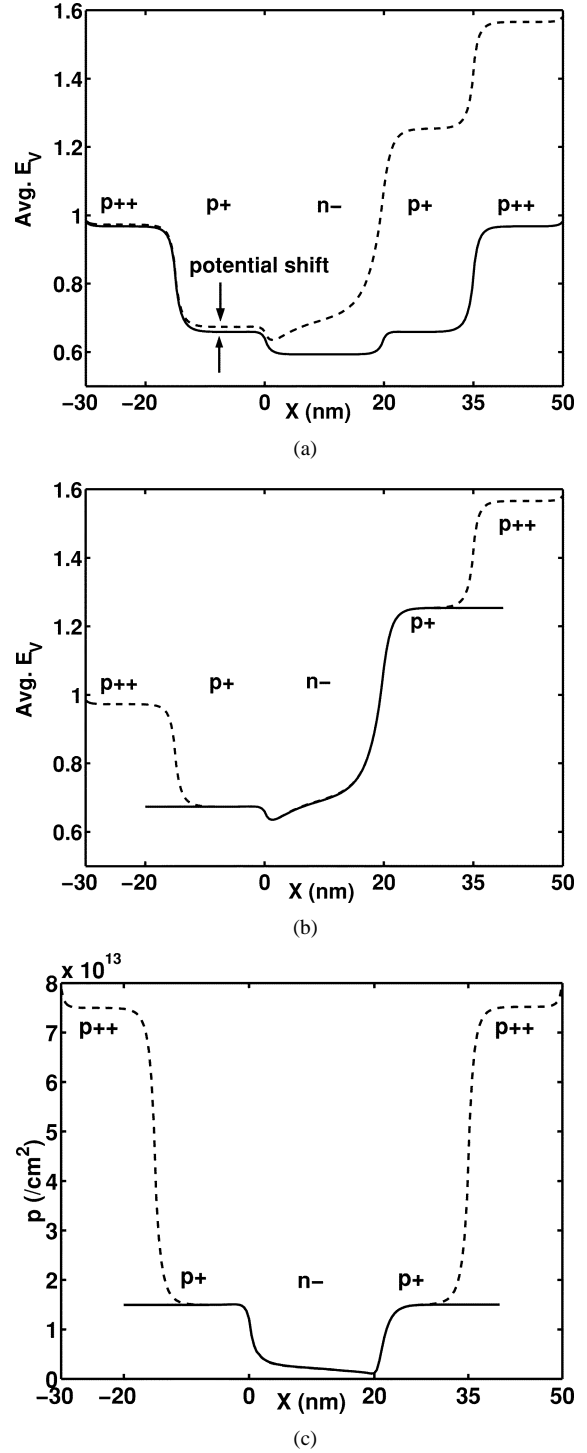


Fig. 10. (a) Average valence band (averaged along z) profile within the p^{++} - p^+ - n^- - p^+ - p^{++} 1.5-nm body transistor in equilibrium ($V_{GS} = -0.6 \text{ V}$) and in the ON state is plotted on the left. On the right, we compare the average valence band obtained using floating boundary conditions (solid line) with that obtained using fixed boundary conditions (dotted line) in the ON state. (b) Charge density profiles obtained by simulating the p^+ - n^- - p^+ device using floating boundary conditions (solid line) compared with those obtained using fixed boundary conditions (dotted line) in the ON state. Note that irrespective of the boundary condition used, macroscopic charge neutrality is always achieved.

drain. Therefore, a fixed potential boundary condition based on charge neutrality can be used when solving Poisson's equation. The p^{++} regions maintain a near-equilibrium distribution even under bias.

On examining the nonequilibrium ($|V_{GS}| = |V_{DS}| = 0.6$ V) potential profile [Fig. 10(a)] of the modified device, it is clear that the averaged valence band is unchanged in the heavily doped p^{++} regions but floats to a higher value in the p^+ source region of the intrinsic device. This observation can be explained by examining Fig. 2. Under equilibrium conditions, both the $+k_x$ and the $-k_x$ states in the p^+ source are filled by a single Fermi level resulting in zero net current. As the drain bias is increased to higher and higher values, the drain injected (negative) half of the hole distribution is suppressed in region 1 (empty circles in Fig. 2). Therefore, all of the charge in this region is comprised of source injected carriers. Note that with increasing V_{GS} , the source-to-channel barrier height decreases. This reduces the fraction of the source injected carriers that is reflected back and most of the charge in region 1 exists in the $+k_x$ states. Although nearly one half of the \vec{k} -space occupancy is suppressed, 2-D electrostatics requires that charge neutrality must be maintained (integrated doping equals the 2-D hole density) at every point within region 1. To achieve charge neutrality, the hole density residing in the $+k_x$ states in region 1 nearly doubles between the equilibrium and nonequilibrium bias conditions. To accommodate this increased charge in the $+k_x$ half, the valence band has to float to a higher energy [Fig. 10(a)]. Increased occupancy of the high-energy $+k_x$ states is what we refer to as degeneracy. Carriers in the heavily doped p^{++} region are predominantly backscattered by the built-in barrier, so the potential in this region is unchanged with drain bias.

Now, if we remove the p^{++} regions but use the floating boundary condition to terminate the p^+ regions, we observe the potential behavior plotted in Fig. 10(a). Fig. 10(a) demonstrates that the averaged valence band under bias for the device with floating boundaries ($p^+-n^-+p^+$) is identical to that for device with fixed boundaries ($p^{++}-p^+-n^-+p^+-p^{++}$) within the region of interest ($p^+-n^-+p^+$). 2-D charge density profiles also exhibit a similar match in the $p^+-n^-+p^+$ region [Fig. 10(b)], thus indicating that the floating boundary condition does capture the effect of coupling a ballistic device to a scattering contact.

V. SUMMARY

This paper described a self-consistent 2-D simulation scheme for modeling ballistic transport in ultra-thin-body fully depleted SOI pMOSFETs including the effect of band nonparabolicity. While doing so, the use of floating boundary conditions was highlighted and validated. The simulator was used to examine the physics of subband engineering on hole transport. Our simulations indicate that under conditions of single subband occupancy, the ballistic nMOSFET will significantly outperform the ballistic pMOSFET. They also indicate that 2-D effects are strong in these short-channel devices and need to be accounted for to obtain an accurate ballistic limit. Subband engineering (thinning the SOI film) improves the performance of ballistic nMOSFETs significantly, because both gate capacitance and injection velocity are increased. For ballistic pMOSFETs, the inversion capacitance is increased, but there is a small degradation in the hole injection velocity. Hence the performance im-

provement is significantly smaller. The heavy hole band flux is higher along $\langle 110 \rangle$ as compared to the $\langle 100 \rangle$ direction for a given charge density. The reversed trend applies to the light hole subbands. Therefore, if most of the hole charge is in the heavy hole band, a channel orientation of $\langle 110 \rangle$ yields a higher current as compared to a $\langle 100 \rangle$ channel orientation. If the light hole population increases, this difference is reduced and channel orientation does not affect pMOSFET device performance significantly.

Although we have used a simple treatment of the valence bands, the behavior of the hole current with respect to channel orientation presented in this paper is consistent with a more rigorous treatment which uses a 6×6 Luttinger Hamiltonian to describe the hole band structure [22]. The ideas presented in this paper can be extended to treat ballistic transport including the effect of warped band structures in general. To do so, the analytical calculations for hole density and current will have to be replaced by numerical calculations. We believe that rigorous solutions are definitely desirable and need to be developed to understand the physics of hole transport in SOI transistors, but we feel that simple approaches such as ours provides valuable insight efficiently until rigorous solutions are rendered tractable. The results presented in this paper point out the importance of a careful treatment of the valence band structure when simulating pMOSFETs.

ACKNOWLEDGMENT

The authors would like to thank U. Savagaonkar and P. Damle for useful discussions.

REFERENCES

- [1] Intel Corp. (2001). [Online]. Available: <http://www.intel.co/labs>
- [2] H. Wong, D. Frank, and P. Solomon, "Device design considerations for double gate, ground-plane, and single-gated ultra-thin SOI MOSFETs at the 25-nm channel length generation," in *IEDM Tech. Dig.*, 1998, pp. 407–410.
- [3] Int. Technology Roadmap for Semiconductors. (2001). [Online]. Available: <http://www.itrs.net>
- [4] Z. Ren, R. Venugopal, S. Datta, M. S. Lundstrom, D. Jovanovic, and G. Fossum, "The ballistic nanotransistor: A simulation study," in *IEDM Tech. Dig.*, 2000, pp. 715–718.
- [5] Y. Naveh and K. K. Likharev, "Modeling of 10-nm-scale ballistic MOSFETs," *IEEE Electron Device Lett.*, vol. 21, pp. 242–244, May 2000.
- [6] A. Svizhenko, M. Anantram, T. Govindan, B. Biegel, and R. Venugopal, "2-D quantum mechanical modeling of MOSFETs using the non equilibrium green's function approach," *J. Appl. Phys.*, vol. 91, pp. 2343–2354, 2002.
- [7] D. Frank, Y. Taur, and H. Wong, "Generalized scale length for two-dimensional effects in MOSFETs," *IEEE Electron Device Lett.*, vol. 19, pp. 385–387, Oct. 1998.
- [8] S. Takagi, I. Koga, and A. Toriumi, "Subband structure engineering for performance enhancement of Si MOSFETs," in *IEDM Tech. Dig.*, 1997, pp. 219–222.
- [9] I. Balslev and P. Lawaetz, "On the interpretation of the observed hole mass shift with uniaxial stress in silicon," *Phys. Lett.*, vol. 19, pp. 6–7, 1965.
- [10] S. Rodriguez, J. Villanueva, I. Melchor, and I. Carceller, "Hole confinement and energy subbands in a silicon inversion layer using the effective mass theory," *J. Appl. Phys.*, vol. 86, pp. 438–444, 1999.
- [11] T. Ando, A. Fowler, and F. Stern, "Electronic properties of two-dimensional systems," *Rev. Mod. Phys.*, pp. 437–672, 1982.
- [12] R. Venugopal, Z. Ren, D. Jovanovic, S. Datta, and M. S. Lundstrom, "Simulating quantum transport in nanoscale MOSFETs: Real versus mode space approaches," *J. Appl. Phys.*, vol. 92, pp. 3730–3739, 2002.

- [13] C. Hu, S. Banerjee, K. Sadra, B. Streetman, and R. Sivan, "Quantization effects in inversion layers of pMOSFETS on Si (100) substrates," *IEEE Electron Device Lett.*, vol. 17, pp. 276–278, June 1996.
- [14] C. Moglestue, "Self-consistent calculation of electron and hole inversion charges at silicon–silicon dioxide interfaces," *J Appl. Phys.*, vol. 59, pp. 3175–3183, 1986.
- [15] P. V. Halen and D. L. Pulfrey, "Accurate, short series approximations to Fermi–Dirac integrals of order $-1/2$, $1/2$, 1 , $3/2$, $2,5/2$, 3 , and $7/2$," *J. Appl. Phys.*, vol. 57, pp. 5271–5274, 1985.
- [16] G. W. Brown and B. W. Lindsay, "The numerical solution of Poisson's equation for two-dimensional semiconductor devices," *Solid-State Electron.*, vol. 19, pp. 991–992, 1976.
- [17] D. J. Rose and R. E. Bank, "Global approximate newton methods," *Numer. Math.*, pp. 279–295, 1981.
- [18] Z. Ren, "Thesis," Ph.D., Purdue University, 2001.
- [19] K. Natori, "Ballistic metal–oxide–semiconductor field-effect transistor," *J. Appl. Phys.*, vol. 76, pp. 4879–4890, 1994.
- [20] H. Sayama, Y. Nishida, H. Oda, T. Oishi, S. Shimizu, T. Kunikiyo, K. Sonoda, Y. Inoue, and M. Inuishi, "Effect of $\langle 100 \rangle$ channel direction for high performance SCE immune pMOSFET with less than $0.15 \mu\text{m}$ gate length," in *IEDM Tech. Dig.*, 1999, pp. 657–660.
- [21] J. Rhew, Z. Ren, and M. S. Lundstrom, "A numerical study of ballistic transport in a nanoscale MOSFET," *Solid State Electron.*, vol. 46, pp. 1899–1906, 2002.
- [22] A. Rahman and M. S. Lundstrom, unpublished.

Ramesh Venugopal was born in Chennai, India. He received the Ph.D. degree in electrical and computer engineering from Purdue University, West Lafayette, IN, in 2003.

He is currently with Texas Instruments, Incorporated, Dallas, TX. He works on device physics, design, and simulation.



Zhibin Ren was born in Zhenzhou, China. He received the Ph.D. degree in electrical and computer engineering from Purdue University, West Lafayette, IN, in 2001.

He is currently with IBM, Hopewell Junction, NY. He works on device characterization, physics and simulation.

Mark S. Lundstrom (S'80–SM'80–F'94) received the B.S.E.E. and M.S.E.E. degrees from the University of Minnesota, Minneapolis, in 1973 and 1974, respectively, and the Ph.D. degree from Purdue University, West Lafayette, IN, in 1980.

He joined the faculty of Purdue University in 1980. He is currently the Scifres Distinguished Professor of Electrical and Computer Engineering at Purdue, where he also directs the National Science Foundation Network for Computational Nanotechnology. He previously served as Director of the Optoelectronics Research Center and Assistant Dean of the Schools of Engineering. Before attending Purdue, he was with Hewlett-Packard Corporation working on integrated circuit process development and manufacturing. His current research interests center on the physics of semiconductor devices, especially nanoscale transistors. His previous work included studies of heterostructure devices, solar cells, heterojunction bipolar transistors and semiconductor lasers.

Dr. Lundstrom is a Fellow of the American Physical Society and the recipient of several awards for teaching and research, most recently the 2002 IEEE Cledo Brunetti Award and the 2002 Semiconductor Research Corporation Technical Achievement Award for his work with his colleague S. Datta on nanoscale electronics.